Studies of Flow Characteristics of Injected Jet Fuel under Supercritical Conditions

Thammarat Duangthip[1]*, Jamie S. Ervin[2]

[1]Department of Mechanical Engineering, Asian University of Science and Technology,
89 Moo 12, Highway 331, Huay Yai, Banglamung, Chonburi 20260, Thailand
Tel: 0-3875-4450, Ext 2759, Fax: 0-3875-4460, *E-mail: thammaratd@asianust.ac.th
[2]University of Dayton Research Institute, 300 College Park, Dayton, OH 45469-0210, USA
Tel: 937-252-8878 Fax: 937-252-9917, E-mail: jamie.ervin@notes.udayton.edu

Abstract

At temperatures above 400 °C and at fuel system pressures, JP-8 and Jet A jet fuels exist as supercritical fluids. Fuel nozzles operating under conventional aircraft (subcritical) conditions atomize liquid fuel streams into droplets. The physical injection and mixing mechanisms associated with a nozzle operating under supercritical conditions are very different from those occurring under subcritical conditions. Nevertheless, the studies of jet fuel injection under supercritical conditions are rare. Moreover, little information is known about the physical and chemical characteristics of jet fuel injected under these conditions. The current research examines the flow of fuel at supercritical conditions through a simple nozzle into a region that is also at supercritical conditions. Schlieren images of supercritical jet fuel exiting a simple nozzle into an optical chamber are presented. Computational fluid dynamics simulations of the flow were performed using n-decane as a surrogate fuel. From the results of computational fluid dynamics simulations, it was found that n-decane is a reasonable surrogate for Jet A fuel in calculations as the predicted jet length and spreading angle are found to agree well with measurements obtained from the recorded images. In addition, it was found that the penetration depth of a supercritical jet into the optical chamber is less than that for a subcritical jet with the same fuel mass flow rate and pressure conditions.

Key Words: Jet fuel, Supercritical conditions, Flow visualization, Numerical simulation.

1. Introduction

Fuel is the primary cooling medium in high-performance aircraft. Advanced aircraft are expected to have cooling demands which require jet fuel to exist at temperatures above the critical temperature before injection into the combustor. Thus, future gas turbine engines will require the injection of fuel existing at a supercritical thermodynamic state into an environment that is also above the critical point of the fuel. At temperatures above approximately 400 °C and at fuel system pressures, the primary fuel of the U.S. Air Force, JP-8, or jet fuels like JP-8 and Jet A exist as a supercritical fluid with gas-like diffusivity and viscosity [1]. Under supercritical temperature conditions, pyrolytic reactions within heated jet fuel become dominant. Chemical changes, such as fuel pyrolysis, are controlled by physical characteristics of the fuel and the fuel system. The involved fluid dynamics and heat transfer vary during flight and change the location of maximum thermal gradients and maximum chemistry. Thus, it is important to understand the fundamental physical and chemical processes which occur for hydrocarbon fuels existing under supercritical conditions.

For purposes of combustion, fuel nozzles operating under conventional aircraft (subcritical) conditions atomize liquid fuel streams into small, uniformly-sized droplets with the desired spray angle. Under supercritical conditions, the fuel exits the nozzle as a gas-like fluid rather than as a multitude of droplets, and there can be large variations in fuel density, specific heat, speed of sound, viscosity, and thermal conductivity [2]. Thus, the physical injection and mixing mechanisms associated with a nozzle operating under supercritical conditions are very different from those occurring under subcritical conditions.

Previous research considered the injection of ethylene which was initially at supercritical conditions into a large chamber filled with nitrogen at constant temperature and subcritical pressures [3, 4]. The goal was to examine the effects of transport properties near the critical point on shock structure, jet appearance, and flow choking. Others have studied the injection of liquid jets injected into supercritical conditions [2, 5, 6, 7, 8]. It is also desirable to conduct experiments in which a supercritical fluid is injected into surroundings under supercritical conditions. Knowledge of injection processes into surroundings at supercritical conditions is important because supercritical conditions will exist in the combustion chamber of advanced aircraft [1]. In some of their experiments,

Chehroudi et al. [2] and Chen and Sui [8] injected fluids initially at supercritical conditions into surroundings that were also at supercritical pressures and temperatures (relative to the injected fluid). Chehroudi et al. [2] injected pure N_2, He, and O_2 into a high pressure chamber containing either N_2, He, or mixtures of CO and N_2. Chen and Sui [8] studied the injection of SF_6 injected into a chamber filled with stagnant N_2 or CO_2 at high pressure. Much of their work focused on subcritical injection very near the critical point of SF_6. Unfortunately, there is little available in the literature concerning the injection of an initially supercritical hydrocarbon fuel into supercritical conditions [9]. The relatively high critical temperatures and pressures associated with common hydrocarbon fuels necessarily make injection studies at supercritical conditions difficult. Previous studies involving supercritical fluid injection largely consider studies of droplets and sprays. Studies involving jets of supercritical fluids are relatively rare and, thus, more research involving injection of supercritical fluids is needed [2, 9].

In the current work, Jet A fuel initially at supercritical conditions is injected into an environment with pressures and temperatures above the critical pressure and temperature of the fuel. In addition, the Jet A fuel is in co-flow with N_2 gas. (In this work, supercritical refers to the critical condition of the fuel.) In order to better understand the mixing and injection processes, schlieren imaging is used. It is believed that these are the first images of supercritical jet fuel exiting a nozzle into a chamber which is also at supercritical conditions. Computational fluid dynamics simulations are performed using a simple surrogate fuel for purposes of comparison with the images of Jet A. The results of this work can be used to assist further development of computational models for engine designers to simulate fuel flowing through nozzles at supercritical conditions.

2. Experimental

Jet A fuel is similar to both JP-8 and Jet A-1 jet fuels, but Jet A has a higher freeze point temperature specification [10]. JP-8 is essentially Jet A-1 with three additives: a lubricity improver/corrosion inhibitor, an anti-static additive, and an icing inhibitor. In addition, Jet A and Jet A-1 are used as commercial aviation fuels. In this study, a Jet A fuel sample (designated as F3219 was additized and then injected into an optical chamber for purposes of flow visualization. Additives combined with the neat fuel include those given by MIL-T-83133D (JP-8 fuel specification) and a proprietary thermal stability additive (Betz Dearborn 8Q462) used in the JP-8+100 Program. This additive was found to reduce thermal-oxidative surface deposition significantly below that of the neat fuel in most fuel test devices [11]. Dissolved O_2 within heated jet fuel is responsible for thermal-oxidative fuel degradation and surface deposit formation. Since it was desired to eliminate surface deposition, gaseous N_2 was bubbled through the fuel to reduce the dissolved O_2 concentration within the fuel. A gas chromatograph verified that the dissolved O_2 concentration of the fuel before heating was less than 1 ppm (w/w) and, thus, ensured that minimal thermal-oxidative surface deposition would occur. The fuel was heated in a flow rig which uses two different types of heaters [12]. The first consists of a heated copper block. The block is comprised of two cylindrical halves which have a 7.62-cm diameter and a 45.7-cm length. The cylindrical pieces, when clamped together, form a near-interference fit about the stainless-steel tubing through which the fuel passes. Each half contains a 1,500-Watt cartridge heater, and a thermocouple embedded within one of the halves provides a temperature signal to the controller for the cartridge heaters. The second kind of heater is a split-tube furnace (7,980 Watt) that is mounted vertically and employs radiant heating. It has an active length of 61.0-cm and a 12.7-cm interior diameter. In addition, the furnace employs K type thermocouples for control purposes. The pressure in the copper block and furnace was held near 2.7 MPa by the use of a pump and flow control valves such that the fuel entered the copper blocks as a liquid and transitioned to a supercritical fluid within the furnace. After passing through the heated block and furnace, the fuel flowed through a nozzle. The nozzle (Figure 2) consists of a (316) stainless-steel tube (12.7 mm length x 1.6 mm OD x 0.3 mm ID) welded to a larger tube (The 3.2 mm OD x 1.4 mm ID fuel line tube was drilled to an ID of 1.6 mm and depth of 6.35 mm to accommodate the smaller tube.). Fuel passed from the nozzle into the optical chamber (Figure 3) in (vertical downward) co-axial flow with heated N_2. The flowing N_2 (3.6 g/s) was heated by another furnace to produce a high nozzle wall temperature. In addition, for safety purposes the N_2 served to reduce the probability of ignition. Moreover, injected fuel in actual aircraft is often in co-axial flow with an air stream. The optical chamber experiments has quartz windows (5.08-cm x 10.16-cm) on two sides for optical access and allow a maximum pressure of 3.45 MPa. Feed-throughs permit insertion of two type K thermocouples (1.5 mm diameter), and the pressure was measured using a pressure transducer. Thermocouples (20 gage) welded to the outer surface of the chamber provided outer wall temperatures with an uncertainty of $\pm$2 C. The fuel mass flow rate was fixed at either 0.2 g/s or 0.4 g/s. In these experiments, fuel and N_2 temperatures upstream of the nozzle, fuel and N_2 mixture temperature below the nozzle, chamber wall temperature, and fuel and N_2 flow rates were measured. Individual experiments were run for short times (~15 minutes) to minimize surface deposition. A water-cooled heat exchanger reduces the temperature of the fuel to near ambient conditions after the fuel exits the test section. Cooling the fuel allows safe sample collection and extends the life of the tube downstream of the heat exchanger.

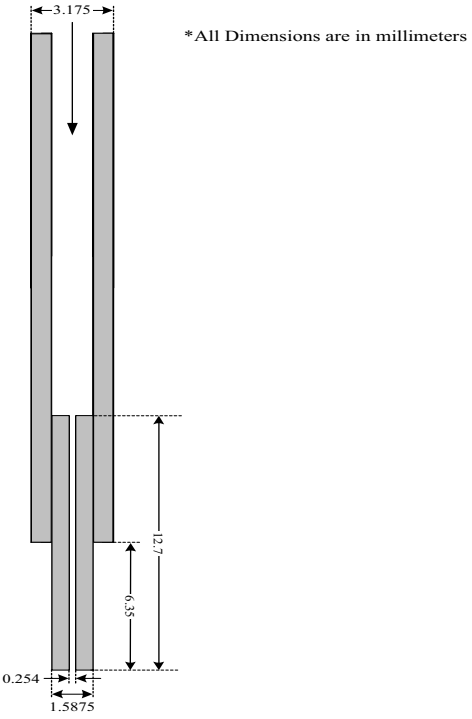

Figure 2. Nozzle used in flow visualization studies

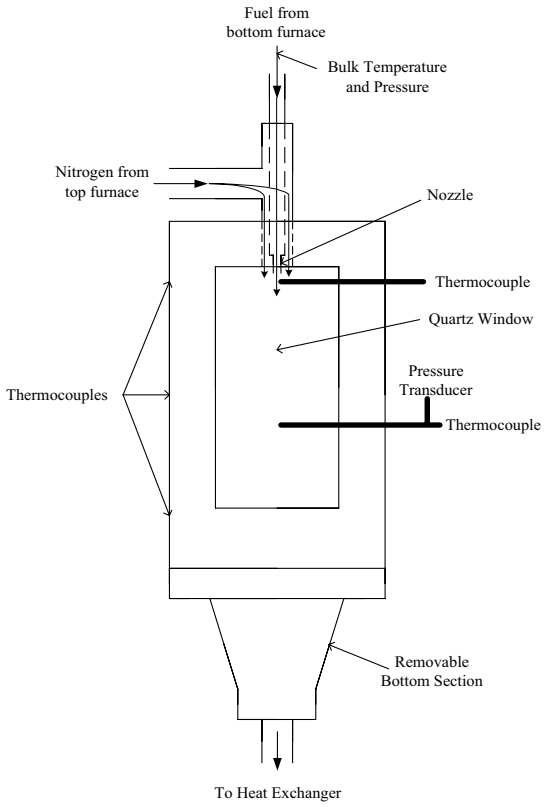

Figure 3. Optical chamber used in flow visualization

Near the exit of the system, fuel is diverted to a gas/liquid separator. Separation allows gas product samples to be analyzed off-line using a GC-FID/TCD system. The liquid portion of the stressed fuel is analyzed by conventional GC-MS techniques. Beyond the gas/liquid separator, the fuel exits to a scrap tank. In the experiments performed here, products of thermal cracking reactions were essentially immeasurable. Thus, it can be reasonably assumed that there was little pyrolysis of the fuel. At supercritical conditions, fuel exiting the nozzle is visible neither to the naked eye nor to white light photography. For this reason, a schlieren optics arrangement was used for flow visualization [13]. Light emanating from a Xenon flash lamp passes through a condenser and focusing lens and is then redirected by a 45° flat mirror to a parabolic mirror (152.4-cm focal length x 15.2-cm diameter). The parabolic mirror then directs the parallel light rays through the test section. Other mirrors direct the detected light such that a knife edge blocks a portion of the light entering the camera. An image of the flow pattern is recorded using a CCD camera (Panasonic GPUS502, three interline transfer CCDs with 768 x 494 pixels) connected to a (Mitsubishi HSU770 SVHS) VCR. An image is captured using a frame grabber (Matrox Marvel G400) connected in series with the VCR. Two sequential images are averaged for each condition reported.

3. Numerical Model

Computational fluid dynamics simulations assist the interpretation of flow visualization studies and extend the study of phenomena for which experimental techniques are either unavailable or limited. To simulate the injection of supercritical fuel into a supercritical environment, the species, temperature, and velocity distributions were obtained by finite volume solution of the species, enthalpy, Navier-Stokes, and turbulent energy equations. The time dependent governing equations written in the cylindrical (z,r) coordinate system for axisymmetric flow are

$$\frac{\partial \rho}{\partial t} + \frac{\partial \rho u}{\partial z} + \frac{\partial \rho v}{\partial r} + \frac{\rho v}{r} = 0 \qquad (1)$$

$$\frac{\partial \rho\Phi}{\partial t} + \frac{\partial \rho u\Phi}{\partial z} + \frac{\partial \rho v\Phi}{\partial r} = \frac{\partial}{\partial z}\left(\Gamma^{\Phi}\frac{\partial \Phi}{\partial z}\right) + \frac{\partial}{\partial r}\left(\Gamma^{\Phi}\frac{\partial \Phi}{\partial r}\right) - \frac{\rho v\Phi}{r} + \frac{\Gamma^{\Phi}}{r}\frac{\partial \Phi}{\partial r} + S^{\Phi} \qquad (2)$$

Equation 1 is the continuity equation, and Equation 2 represents the momentum, species, or energy equation depending on the variable represented by Φ. Table 1 lists the transport coefficients Γ^{Φ} and the source terms S^{Φ} of the governing equations. Buoyancy forces were included in the simulations, and the gravity vector is in the same direction as theflow from the nozzle. The fuel exiting the nozzle has Reynolds numbers (from 12,000 to 23,000) that are characteristic of turbulent jet flows (Re is defined as $\rho UD/\mu$). In contrast, the Reynolds number at the fuel nozzle exit of the nitrogen in co-flow with the jet fuel

was relatively low (on the order of 2000). The standard k-ε turbulence model [14] has been used previously in supercritical and transcritical studies to provide reasonable predictions of the evolution of an O_2 jet [15]. In preliminary work here, there were negligible differences between calculations of the spreading angle, jet length, and velocities which used the standard k-ε turbulence model and those which employed the low Reynolds number k-ε model of Chien [16]. In addition, it was found that calculations which used the low Reynolds number k-ε turbulence model required only one-half the computational time used by the standard k-ε model.

Thus, in this physical arrangement which involved simultaneously occurring high and low Reynolds number flows, a low Reynolds number k-ε model was used in all the calculations presented. Since the fuel (Re of 12,000 to 23,000 at the location where the fuel is injected into the optical chamber) and N_2 flows are turbulent, the rate of turbulent mass transport is several orders of magnitude greater than that of the concentration-driven (molecular-diffusive) mass transport. Thus, a constant Schmidt number of unity was used for simplicity. Values of the constants used in the model of turbulent species transport are listed in Table 1 and in the nomenclature. The governing equations were solved sequentially using the commercially available CFD-ACE computational fluid dynamics code [17]. Convective terms were represented by a second order accurate upwind scheme, and a version of the SIMPLEC algorithm was used in the solution procedure [17]. The grid system of Figure 4 which contains 89 cells in the radial direction and 200 cells in the axial direction is used in most simulations. Because the nozzle ID (0.3 mm) is significantly smaller than either the chamber width (50.8 mm) or length (101.6 mm), it was assumed that the flow near the chamber walls does not significantly affect the flow near the nozzle outlet. Thus, the rectangular shape of the actual chamber was (as a first order approximation) adequately represented by a two-dimensional axisymmetric (structured) grid. Since the behavior of the fuel jet near the nozzle exit is of primary interest, the length of the computational grid is one-fourth of the chamber length (25.4 mm). The length in the radial direction of the computational grid is 25.4 mm. Computational cells are clustered within the shear layer between the N_2 and fuel. In other regions, the orthogonal grid system has expanding cell sizes in both z and r directions. Near the walls, the first cell was located at a y+ distance less than 5. Large gradients in temperature, velocity, or species are not expected in the far field away from the fuel and N_2 jets under the present flow conditions. From the physical arrangement, the greatest changes in the flow variables are expected to be near the co-annular passage (Figure 4). Thus, a grid study was performed in which the grid density was increased in the fuel nozzle (6 cells to 12 cells), the region where the n-decane and N_2 are mixed (19 cells to 38 cells), and the N_2 inlet (20 cells to 40 cells). In addition, the total number of cells in the axial (main flow direction) direction was increased (200 cells to 300 cells). The computational grid of Figure 4 was refined differently in different regions because of the grid non-uniformity. Solutions for species, temperature, and velocities changed little (less than 2%) with the use of the fine grid. In addition, the differences between the calculated spreading angles and penetration depths resulting from use of the coarse and fine grids were immeasurable. Thus, to have a more practical computational time, the coarse grid was used for the calculations presented in this work.

With regard to boundary conditions, the flow has zero velocity at solid surfaces. At the upper boundary of the grid (Figure 4), the velocity profiles of the entering nitrogen and fuel are assumed to be uniform for simplicity. Entering fuel and nitrogen temperatures, as well as the wall temperatures were obtained from the experiments and are used as boundary conditions. In addition, the measured pressure level at the inlet was known. Along the bottom of the grid (Figure 4), an outflow boundary condition which employs a simple extrapolation procedure [17] is used to determine the unknown variables there. The calculations were initiated with a uniform flow of N_2 everywhere, and then the fuel flow is switched on. After the residuals were reduced below four orders of magnitude from their maximum value, the solution was considered to be converged.

Jet fuel is a complex mixture of a multitude of hydrocarbon species. For purposes of simulating the fluid dynamics involving a jet fuel, it is reasonable to use a simple representative fuel. Here, n-decane was selected as a surrogate fuel because it has a critical temperature and pressure (T_c = 344.55 $\pm$ 0.6 °C, P_c = 2.11 $\pm$ 0.05 MPa) [18] similar to the pseudo-critical temperature and pressure of the selected Jet A sample. The pseudo-critical temperature and pressure for this fuel sample were estimated (T_c = 368 °C P_c = 1.96 MPa) using correlations described elsewhere [19]. Edwards and Maurice suggest that a single component surrogate fuel that has a critical temperature near the pseudo-critical temperature of a selected jet fuel can be used to adequately represent the actual jet fuel in simulations of non-reacting flows (which do not have liquid-to-vapor phase change) [10]. The commercial solver was modified to calculate supercritical thermodynamic and transport properties of mixtures of n-decane and N_2 as a function of the local pressure and temperature within the computational cells using SUPERTRAPP FORTRAN subroutines. With SUPERTRAPP, the phase compositions were calculated using the Peng-Robinson equation of state [20], and the properties were determined by a NIST extended corresponding states model which uses propane as a reference fluid [21]. SUPERTRAPP is known to provide well-behaved thermodynamic properties near the critical point [21]. Table 2 shows representative values of thermodynamic and transport properties for mixtures of

N_2 and n-decane for temperatures and pressures for which n-decane is a supercritical fluid.

Table 1. Source term and transport coefficients in Eq. (2)

Φ	Γ^{Φ}	S^{Φ}
u	$\mu + \mu_t$	$-\frac{\partial P}{\partial z}+\frac{\partial}{\partial z}\left(\Gamma^u \frac{\partial u}{\partial z}\right)+\frac{\partial}{\partial r}\left(\Gamma^u \frac{\partial v}{\partial z}\right)+\frac{\Gamma^u}{r}\frac{\partial v}{\partial z}+\rho g$
v	$\mu + \mu_t$	$-\frac{\partial P}{\partial r}+\frac{\partial}{\partial z}\left(\Gamma^v \frac{\partial u}{\partial r}\right)+\frac{\partial}{\partial r}\left(\Gamma^v \frac{\partial v}{\partial r}\right)+\frac{\Gamma^v}{r}\frac{\partial v}{\partial r}+2\Gamma^v$
k	$\mu+\frac{\mu_t}{\sigma_k}$	Standard k-ε, $G-\rho\varepsilon$
		Low Re k-ε, $C_{\varepsilon_1} f_1 \frac{G\varepsilon}{k} - C_{\varepsilon_2} f_2 \rho \frac{\varepsilon^2}{k} + E$
ε	$\mu+\frac{\mu_t}{\sigma_\varepsilon}$	Standard k-ε, $C_1 G\frac{\varepsilon}{k} - C_2 \rho \frac{\varepsilon^2}{k}$
		Low Re k-ε, $C_1 G\frac{\varepsilon}{k} - C_2 \rho \frac{\varepsilon^2}{k}$
h	$\frac{k}{c_p}+\frac{\mu_t}{\sigma_h}$	0
Y_i	$\rho D_i + \frac{\mu_t}{\sigma_{Y_i}}$	$\dot{\omega}_i$

$$G = \mu_t \left[2\left\{ \left(\frac{\partial u}{\partial z}\right)^2 + \left(\frac{\partial v}{\partial r}\right)^2 + \left(\frac{v}{r}\right)^2 \right\} + \left(\frac{\partial v}{\partial z} + \frac{\partial u}{\partial r}\right)^2 \right]$$

$f_1 = 1.0$, $f_2 = 1 - 0.22 \exp[-(\mathrm{Re}/6)^2]$, $E = -2\nu(\varepsilon / y^2) \exp(-0.5\, y^+)$,

$D = 2\nu k / y^2$, $C_{\varepsilon_1} = 1.35$, $C_{\varepsilon_2} = 1.8$, $\mu_t = C_\mu \rho k / \varepsilon$

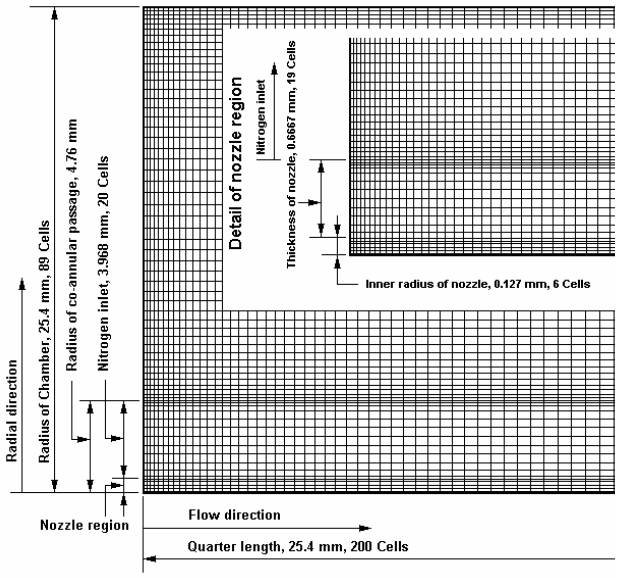

Figure 4. Computational grid

Table 2 Properties of *n*-decane/nitrogen mixtures for different temperatures, pressures, and mole fractions calculated using SUPERTRAPP

Temp, K (°C)	Pres (MPa)	$C_{10}H_{22}$ Mole Fraction	N_2 Mole Fraction	Density (kg/m^3)	C_p (kJ/kg K)	μ x 10^{-6} (Ns/m^2)	k x 10^{-2} (W/mK)
713 (440)	3.08	1.0	0.0	107.20	3.52	16.74	5.33
725 (452)	2.65	0.75	0.25	55.10	3.14	16.34	4.30
735 (462)	2.65	0.50	0.50	37.50	2.90	18.66	3.63
745 (472)	2.65	0.25	0.75	23.90	2.47	23.16	3.49

4. Results and Discussion

4.1 Effects of Varying Nozzle Exit Temperature.

For a given pressure, the density and viscosity of a hydrocarbon fuel may vary strongly with temperature. From [26], for a fixed mass flow rate and pressure, the Reynolds numbers of the fuel in Figures 5a, 5b, and 5c increase rapidly with temperature. Upon comparison of Figures 5a, 5b, and 5c, it is observed that the length of the fuel jet decreases as the injected fuel transitions from compressed liquid to supercritical fluid. The decrease in the jet length implies that the fuel and nitrogen are mixed faster than under the subcritical conditions. Under supercritical conditions, the surface tension of the fuel vanishes, and the mixing process does not involve evaporation. Moreover, a supercritical fluid generally has a greater diffusivity and a lower viscosity than a liquid. Together with zero surface tension, these transport characteristics contribute to the relatively more rapid mixing of the supercritical fuel. Thus, the mixing process between the fuel and nitrogen occurs more rapidly for fuel at supercritical conditions and results in less penetration into the chamber than for liquid fuel. The observation that the penetration depth decreases with increasing fuel temperature at supercritical conditions is important for the design of future combustors. Admittedly, the design of gas turbine combustors is complex and depends on many factors.

How ever, a reduced penetration depth implies a reduced mixing time for the fuel jet for otherwise identical circumstances. Passing through the nozzle, jet fuel is heated by N_2 flowing over the nozzle exterior. Upon exiting the nozzle at supercritical conditions, the fuel expands into the chamber forming a gas-like turbulent jet. Within the fuel jet, the fluctuating transverse velocity component enhances transport of unmixed fuel from the core region of the jet to the surrounding fluid. Understanding the mixing dynamics of Jet A and N_2 is complicated by differences in molecular weight, velocity, and temperature. Figure 5 shows a schlieren image of Jet A fuel and N_2 at supercritical conditions (Figure 5a) (fuel mass flow rate of 0.2 g/s, exit nozzle temperature of 441 °C, and pressure of 2.65 MPa) together with plots of predicted density (Figure 5b), mass fraction of n-decane (Figure 5c), and temperature (Figure 6d). Figure 5a (same as Figure 5c in [26]) shows that the fuel jet becomes indistinguishable from the N_2 at a location 7.5 mm (Z/D = 30, where Z is the distance along the jet centerline below the nozzle and D is the nozzle ID) below the fuel nozzle. For non-isothermal cold-into-hot jets, similar Z/D have been observed elsewhere [2, 23]. In addition, Figure 5b shows that axial and radial density gradients have become negligible 7.5 mm below the nozzle. Since schlieren imaging is sensitive to density gradient, Figures 5a and 5b support one another in defining a value for the jet length (7.5 mm). This agreement also shows that it is reasonable to use a simple fuel such as n-decane in numerical simulations of the heat transfer and transport phenomena of a more complex Jet A fuel. At this location 7.5 mm from the nozzle, Figure 5c shows that the mass fraction is less than 0.2. Moreover, Figure 5d shows that the low-temperature (blue) core region of the fuel jet persists for 7.5 mm beyond the nozzle exit. Figure 5d also shows that the temperature of the N_2 away from the fuel jet is nearly uniform. This uniformity indicates that heat loss from the chamber walls to the ambient has little effect on the temperature distribution near the fuel jet.

4.2 Jet growth rate. The fluctuating transverse velocity component of the n-decane jet enhances mixing of fuel from the jet core region with the surrounding N_2 within a mixing layer. The mixing layer grows outward as the heated jet extends further into the chamber. The growth of the mixing layer has been described in terms of an initial jet spreading angle [24]. In Figure 6, the jet spreading angle is measured from the nozzle centerline to a tangent line drawn along the outer portion of the jet mixing layer. The spreading angle of the Jet A jet in the schlieren image of Figure 6a is 3.5° $\pm$ 0.5°, and the spreading angle determined from the calculated density plot for n-decane is Figure 6b is 3.0° $\pm$ 0.5°. Here, the calculated density field resulting from the use of n-decane (nozzle exit temperature 441 °C and N_2 temperature of 506 °C) provides a reasonable prediction of the spreading angle of the supercritical Jet A jet. In addition, Table 3 shows that the spreading angles determined from schlieren images at other conditions compare well with those obtained by numerical simulation.

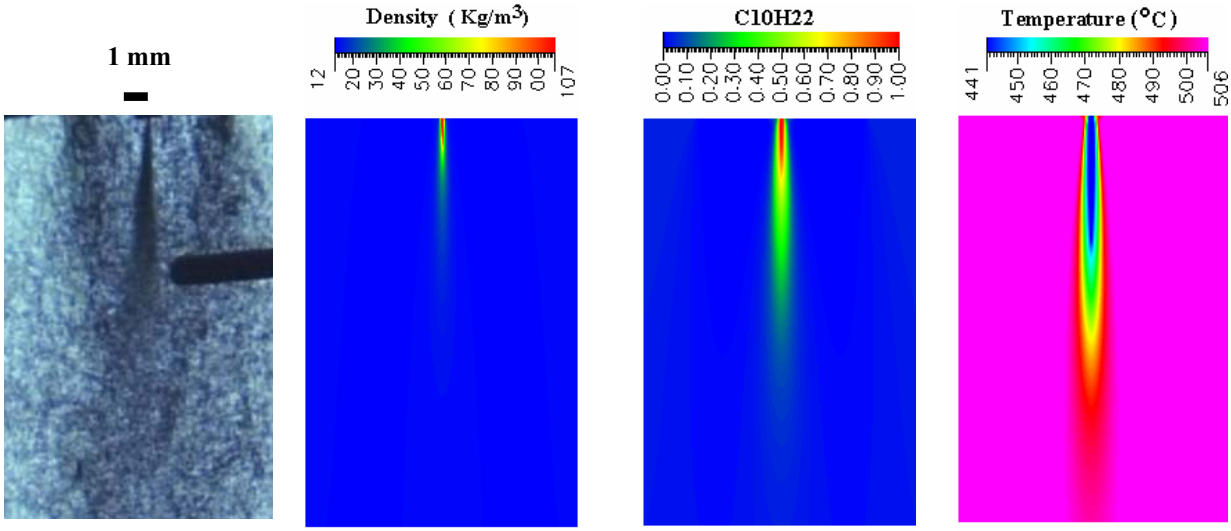

(a) (b) (c) (d)

Figure 5. Jet fuel or *n*-decane at supercritical conditions in coflow with N2. Fuel mass flow rate of 0.2 g/s, inlet nozzle temperature of 441°C, and pressure of 2.65 MPa (Tr = 1.11 and Pr = 1.35). (a) Schlieren image of fuel and N2 (b) Predicted density (kg/m^3) of *n*-decane and N2 mixture. (c) Predicted mass fraction of *n*-decane. (d) Predicted temperature (°C).

Table 3. Predicted and measured spreading angles and jet length (Chamber pressure of 2.65 MPa)

MassFlow Rate (g/s)	Exit Temperature(°C)		Spreading Angle (deg)(± 0.5 deg)		Jet Length (mm)	
	Jet Fuel	N2	Md	Pd	Md	Pd
0. 2	393	510	3. 5	3. 0	12. 0	15. 0
0. 2	441	506	3. 5	3. 0	7. 5	9. 0
0. 2	465	588	3. 5	3. 0	6. 0	7. 0
0. 4	405	588	5. 0	4. 5	15. 0	18. 0
0. 4	424	590	5. 0	4. 5	12. 0	14. 0
0. 4	465	590	5. 0	4. 5	8. 0	9. 0

To confirm the numerical simulations of the co-flow of n-decane and N_2 jets, predictions of the mean fuel mass fraction along the jet centerline are compared to values predicted by a semi-empirical correlation. Time-averaged concentration measurements along the centerlines of variable-density, axisymmetric, turbulent jets formed by the flow of a faster moving gas into a slow coflow of a second gas have been performed by Pitts [23]. Pitts found that equation (3):

$$Y_o/Y_m = (K_c Z)/r_\varepsilon + (\rho_\infty/\rho_o - 1)K \qquad (3)$$

described his time-averaged measurements of the jet mass fraction along the centerline, Y_m [23, 25]. In equation (3), Y_o is the time-averaged mass fraction at the nozzle exit, ρ_∞ is the density of the external, slow moving gas, ρ_o is the density of the faster moving jet at the nozzle exit, Z is the distance from the nozzle exit along the jet centerline, and both K and K_c are constants. The effective radius, r_ε,

is defined as $r_\varepsilon = r_o(\rho_o/\rho_\infty)^{1/2}$, and r_o is the radius of jet nozzle. (In this discussion, Y_o = 1.) Following Pitts, values of K = -0.5 and K_c = 0.114 have been assumed, and values for the global density ratio are from Figure 8b [23]. If our numerical simulations of Y_o/Y_m within the n-decane jet are reasonable, they should follow the predictions of equation (3). Figure 7 shows predictions of Y_o/Y_m for several different jet/coflow pairs as a function of Z/r_o using equation (3) and values from Pitts [23]. The use of several different jet/coflow pairs demonstrates the wide applicability of equation (3). In addition, Figure 9 includes predictions of Y_o/Y_m for the n-decane/N_2 coflow pair from both the use of equation (3) and the present numerical simulations. The solid circular symbols near the n-decane/N_2 curve represent Y_o/Y_m values derived from the current numerical simulations which involve the Reynolds-averaged turbulence equations. Figure 7 shows that there is good agreement between the empirical correlation (equation (3)) and the present simulations. Downstream from the flow development region (> 5-10 diameters) one dimensionless length scale will specify time-averaged concentrations for jet coflow pairs [23].

It has been suggested that the reciprocal of the time-averaged mass fraction along a gaseous jet centerline scales with the following relationship [23, 25]:

$$\frac{Y_o}{Y_m} = K_c\left(\frac{Z - Z_o}{r_\varepsilon}\right) \qquad (4)$$

In equation (4), Z_O is the virtual origin of the jet. (This is the point where the jet centerline intersects a line drawn tangent to the jet exterior. Here, Y_o is unity, and Z_O is negative.) Several experimental studies (isothermal and non-isothermal) support the scaling representation of equation (4) for axisymmetric jets where the coflowing gases have different densities but the downstream density asymptotically becomes constant [25]. Figure 8 shows $1/Y_m$ plotted against $(Z\text{-}Z_O)/r_\varepsilon$ for the present n-decane and N_2 computational fluid dynamics calculations together with measured values for six jet/coflow gas pairs from Pitts [23]. Figure 8 shows that the jet/coflow pairs partially collapse onto a single curve, and this collapse indicates a degree of similarity. Similarity is useful in the fundamental understanding of the fluid dynamics of simple flows. Moreover, the observation that the numerical predictions for n-decane and N_2 tend to fall on a curve common to other coflow pairs provides additional validation of the present calculations.

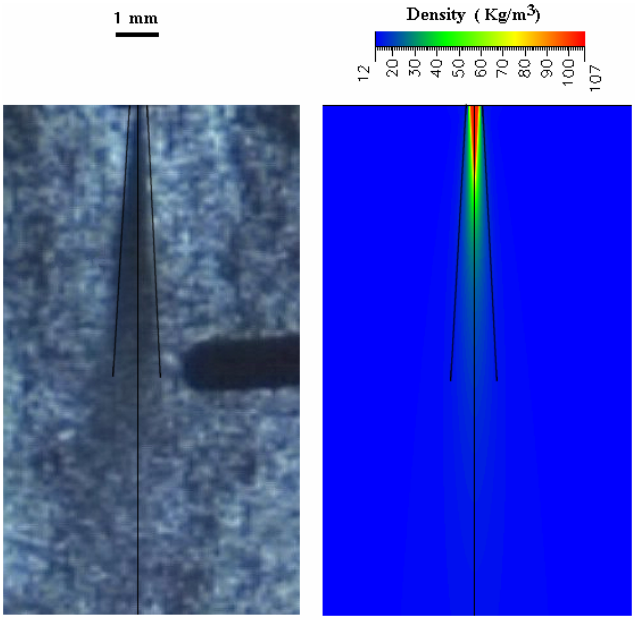

(a) (b)

Figure 6. a) Measured (3.5°) and b) predicted (3.0°) spreading angle for jet fuel and surrogate fuel, *n*-decane.

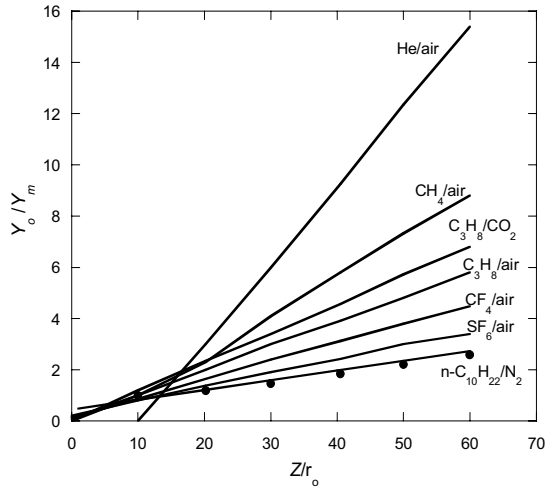

Figure 7. Reciprocal of the mass fraction for different gas pairs. The lines represent the correlation given by Eq. (32). The solid circles are predictions resulting from the present computational fluid dynamics simulations.

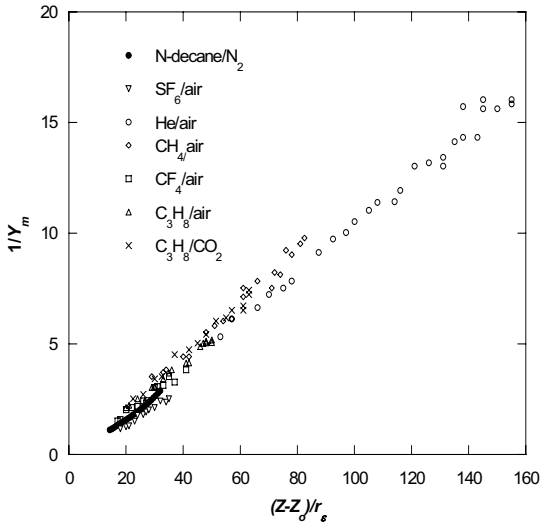

Figure 8. Reciprocal of measured time-averaged mass fraction along gaseous jet centerline for different gas pairs in coflow as a function of dimensionless distance from the virtual origin of the jet (Pitts (1991)

Here, $r_{\varepsilon} = r_0(\rho_O/\rho_\infty)^{1/2}$. In addition, values obtained by computational fluid dynamics simulations for *n*-decane and N_2 are shown.

5. Conclusions

Schlieren images of supercritical jet fuel exiting from a simple nozzle into a supercritical environment were obtained. The jet penetration depth, spreading angle, and phase behavior vary with fuel temperature and mass flow rate which, in turn, can vary considerably during an aircraft mission. The observations that the penetration depth decreases with increasing fuel temperature at supercritical conditions and that the spreading angle increases with increasing mass flow rate are important for the design of future combustors. Numerical simulations that used n-decane as a surrogate fuel for purposes of calculating the jet spreading angle and length agreed reasonably well with the measurements. In addition, the numerical predictions of the jet centerline fuel mass fraction agreed well with established correlations. Thus, n-decane or a similar hydrocarbon surrogate fuel can be used for calculations of the heat transfer and fluid dynamics of non-reacting supercritical jet fuel which has a similar critical temperature and pressure.

Acknowledgment
This work was supported by the U.S. Air Force, Fuels Branch, Propulsion Directorate, Air Force Research Laboratory, Wright-Patterson AFB, OH under contract No. F33615-97-C-2719.

Refferences

[1] Edwards, T., Zabarnick, S., 1993. Supercritical Fuel Deposition Mechanisms. Ind. Eng. Chem. Res., Vol. 32, pp. 3117-3122.
[2] Chehroudi, B., Talley, D., Coy, E., 1999. Initial Growth Rate and Visual Characteristics of Round Jet into a Sub- to Supercritical Environment of Relevance to Rocket, Gas Turbine, and Diesel Engines. Paper AIAA 99-0206, 37th AIAA Aerospace Sciences Meeting and Exhibit, Reno, NV, USA, January 11-14.
[3] Wu, P., Chen, T. H., Nejad, A. S., Carter, C. D., 1996. Injection of Supercritical Ethylene in Nitrogen. J. Propulsion and Power, Vol. 12, pp. 770-777.
[4] Wu, P.K., Shahnam, M., Kirkendall, K.A., Carter, C.D., Nejad, A.S., 1999. Expansion and Mixing Processes of Underexpanded Supercritical Fuel Jets into Superheated Conditions. J. Propulsion and Power, Vol. 15, pp. 642-649.
[5] Newman, J. A., Brzustowski, T.A., 1991. Behavior o a Liquid Jet Near the Thermodynamic Critical Region. AIAA Journal, Vol. 9, pp. 1595-1602.
[6] Woodward, R.D., Talley, D.G., 1996. Raman Imaging of Transcritical Cryogenic Propellants. Paper AIAA 96-0468, 34th AIAA Aerospace Sciences Meeting and Exhibit, Reno, NV, USA, January 15-18.
[7] Mayer, W., Ivancic, B., Schik, A., Hornung, U., 1998. Propellant atomization in LOX/GH2 rocket combustors. Paper AIAA 98-3685, 34th AIAA/ASME/SAE/ASEE Joint Propulsion Conference & Exhibit, Cleveland, OH, USA, July 13-15.
[8] Chen, L.D., Sui, P.C., 1994. Atomization During the Injection of Supercritical Fluid into High Pressure Environment. International Union of Theoretical and Applied Mechanics (IUTAM) Symposia on Droplets and Sprays, Taiwan, December 6-10.
[9] Bellan, J., 2000. Supercritical (and Subcritical) Fluid Behavior and Modeling: Drops, Streams, Shear and Mixing Layers, and Jets and Sprays. Progress in Energy and Combustion Science, Vol. 26, pp. 329-366.
[10] Edwards, T., Maurice, L.Q., 2001. Surrogate Mixtures To Represent Complex Aviation and Rocket Fuels. J. Propulsion and Power, Vol. 17, pp 461-466.
[11] Heneghan, S.P., Zabarnick, S., Ballal, D.R., Harrison III, W.E., 1996. JP-8+100: The Development of High-Thermal Stability Jet Fuel. J. Energy Res. Tech, Vol. 118, pp. 170-179.
[12] Ervin, J.S., Williams, T.F., Hartman, G., 1998. Effect of Test Period on the Rate of Fouling in a Complex Flowing System. Prepr.-Am. Chem. Soc., Div. Petr. Chem., Vol. 43, pp. 373-385.
[13] Eckert, E. R., Goldstein, R. J., 1976. Measurements in Heat Transfer. Hemisphere, Washington D.C., USA.
[14] Launder, B.E., Spalding, D.B., 1974. The Numerical Computation of Turbulent Flows. Comp. Methods Appl. Mech. Eng., Vol. 3, pp. 269-289.
[15] Ivancic, B., Mayer, W., Krulle, G., Bruggeman, D., 1999. Experimental and Numerical Investigation of Time and Length Scales in LOX/GH_2-Rocket Combustors. Paper AIAA 99-2211, 35th AIAA/ASME/SAE/ASEE Joint Propulsion Conference and Exhibit, Los Angeles, June 20-24.
[16] Chien, K.Y., 1982. Predictions of Channel and Boundary Layer Flows with a Low-Reynolds Number Turbulence Model. AIAA J., Vol. 20, pp. 33-38.
[17] CFD Research Corporation, 1998. CFD-ACE Theory Manual Version 5.0, Huntsville, AL., USA.
[18] Ambrose, D., Tsonopoulos, C., 1995. Vapor-Liquid Critical Properties of Elements and Compounds 2. Normal Alkanes. J. Chem. Eng. Data, Vol. 40, pp. 531-546.
[19] Yu, J., Eser, S., 1995. Determination of Critical Properties. Ind. Eng. Chem. Res. Vol. 34, pp. 404-409.
[20] Peng, D.Y., Robinson, D.B., 1976. A New Two-Constant Equation of State. Ind. Eng. Chem., Fundam., Vol. 15, pp. 59-64.
[21]Ely, J. F., Huber, M. L., 1990. NIST Standard Reference Database 4 – NIST Thermophysical Properties of Hydrocarbon Mixtures, Gaithersburg, MD, USA.
[22] Nixon, A.C., Ackerman, G.H., Faith, L.E., Henderson, H.T., Ritchie, A.W., Ryland, L.B., Shryne, T.M., 1967. Vaporizing and Endothermic Fuels for Advanced Engine Applications: Part III, Studies of Thermal And Catalytic Reactions, Thermal Stability, and Combustion Properties of Hydrocarbon Fuels (AFAPL-TR-67-114). Air Force Propulsion Laboratory, Wright-Patterson Air Force Base, Dayton, OH, USA.
[23]Pitts, W.M., 1991. Effects of Global Density Ratio On the Centerline Mixing Behavior of Axisymmetric Turbulent Jets. Exps. Fluid, Vol. 11, pp. 125-134.
[24] Abramovich, G.N., 1963. The Theory of Turbulent Jets; M.I.T. Press: Cambridge, MA, USA.
[25] Pitts, W.M., 1986. Effects of Global Density and Reynolds Number Variations on Mixing in Turbulent, Axisymmetric Jets, Report No. NBSIR 86-3340, National Bureau of Standards, Gaithersburg, MD, USA.
[26] Duangthip, T., Ervin, J. S., Williams, T.F., Bento, J. Studies of Injection of Jet Fuel at Supercritical Conditions. Ind. Eng. Chem. Res. 2002, Vol. 41(23), pp. 5856-5866.

Nomenclature

C*1*	Constant = 1.47
C*2*	Constant = 1.92
$C\mu$	Constant = 0.09
D	Tube diameter, m
D_i	Diffusion coefficient of i-th species, m^2/s
G	$\mu_t\left[2\left\{\left(\frac{\partial u}{\partial z}\right)^2+\left(\frac{\partial v}{\partial r}\right)^2+\left(\frac{v}{r}\right)^2\right\}+\left(\frac{\partial v}{\partial z}+\frac{\partial u}{\partial r}\right)^2\right]$
g	Gravitational acceleration, m/s^2
h	Enthalpy, kJ/kg
k	Thermal conductivity; Turbulent kinetic energy, W/m-K; kJ/kg
K	Constant in equation (3)
K_c	Constant in equation (4)
p	Pressure, MPa
P_{ch}	Chamber pressure, MPa
r	Radial coordinate, m
r_o	Radius of jet nozzle, m
r_ε	Effective radius, m
S^Φ	Source term
u	Axial velocity component, m/s
u_τ	Friction velocity, $(\tau_\omega/\rho)^{1/2}$, m/s
U	Mean velocity, m/s
v	Radial velocity component, m/s
$\dot{\omega}$	Rate of Production of i-th species, kg/m^3-s
y	Normal distance from wall, m
Y_i	Mass fraction of i-th species
Y_o	Time-averaged mass fraction at nozzle exit
Y_m	Time-averaged mass fraction along jet centerline
y+	Dimensionless distance from wall, $\rho y u_\tau/\mu$
z	Axial coordinate, m
Z	Distance from nozzle exit along jet centerline, m
Z_o	Virtual origin of jet, m
Φ	Assigned variable in equations (1)-(2)
Γ^Φ	Transport coefficient
ε	Dissipation rate, kJ/kg-s
ρ	Density, kg/m^3
ρ_∞	Density of external, slow moving gas, kg/m^3
ρ_o	Density of faster moving fuel at nozzle exit, kg/m^3
σ_k	Constant = 1.0
σ_ε	Constant = 1.3
σ_h	Constant = 1.0
σ_{Y_i}	Constant = 1.0
τ_w	Wall shear stress, N/m^2
μ	Absolute viscosity, $N\text{-}s/m^2$
μ_t	Turbulent viscosity, $C_\mu\rho k^2/\varepsilon$, N-s/m